

# The Role of Unmanned Aerial Vehicles (UAVs) in Monitoring Rapidly Occurring Landslides

Servet Yaprak<sup>1</sup>, Omer Yildirim<sup>1</sup>, Tekin Susam<sup>1</sup>, Samed Inyurt<sup>2</sup> Irfan  
Oguz<sup>3</sup>

<sup>1</sup>Geomatics Engineering, Gaziosmanpaşa University, Tokat, Turkey

<sup>2</sup>Geomatics Engineering, Bulent Ecevit University, Zonguldak, Turkey

<sup>3</sup>Soil Science and Plant Nutrition, Gaziosmanpaşa University, Tokat, Turkey

Corresponding author: Samed INYURT, e-mail:samed\_inyurt@hotmail.com

**Abstract:** This study used an unmanned aerial vehicle (UAV) that was designed and produced to monitor rapidly occurring landslides in forest areas. It aimed to determine the location data for the study area using image sensors integrated into the UAV. The study area was determined as the landslide sites located in the Taşlıçiftlik campus of Gaziosmanpaşa University, Turkey. It was determined that landslide activities were on going in the determined study area and data was collected regarding the displacement of materials. Additionally, it was observed that data about landslides may be collected in a fast and sensitive way using UAVs, and this method is proposed as a new approach. Flights took place over a total of five different periods. In order to determine the direction and coordinate variables for the developed model, eight ground control points (GCPs), whose coordinates were obtained using the GNSS method, were placed on the study area. In each period, approximately 190 photographs were investigated. The photos obtained were analyzed using the PIX4D software. At the end of each period, the Root Mean Square and ground sample distance (GSD) values of the GCPs were calculated. Orthomosaic and digital surface models (DSM) were produced for the location and height model. The results showed that max RMS=±3.3 cm and max GSD=3.57 cm/1.40 in. When the first and fifth periods were compared, the highest spatial displacement value  $\Delta S = 111.0$  cm, the highest subsidence value  $\Delta h = 37.3$  cm and the highest swelling value  $\Delta h = 28.6$  cm were measured.

**Keywords:** Unmanned aerial vehicles (UAV); landslides; ground sample distance (GSD); digital surface model (DSM); orthomosaic

## 1. Introduction

Landslides are a worldwide phenomenon that creates dramatic physical and economic effects. They can result in a large number of human deaths. Landslides are generally classified by type of movement (slides, flows, spreads, topples or falls) and type of material (rock, debris or earth). Sometimes more than one type of movement occurs within a single landslide. Rockslides and other types of slides involve the displacement of the material along one or more surfaces. The slip may extend downward and outward along a large planar surface, or it may rotate along a concave upward cutting surface. Sometimes, a slip can occur through structural features such as the interface between the resistive bedrock and the weaker top material. A landslide can start with a slow deformation and a superficial soil breakdown on a steep slope; then, superficial damage occurs. After that, the movement of the earth mass accelerates, disintegrates, drifts and grows, and the stream becomes an avalanche-like debris (Hungry et al., 2014). Changes in slope morphology (Di Crescenzo & Santo, 2005; Guadagno et al., 2005; Montgomery & Dietrich, 1994), geological and structural conditions, mechanical properties of soils (De Vita et al., 2012; Moser & Hohensinn, 1983; Moser, 2002), weathering (Calcaterra et al., 2000; Calcaterra & Parise, 2005), weather conditions, hydrological and

hydrogeological conditions (Casagli et al., 2006; Crosta et al., 2003; Iverson & Major, 1986) and changes in land use (Begueria, 2006; Guadagno et al., 2003; Glade, 2003) triggers shallow landslide movements (Cevasco et al., 2013).

Surface soil erodibility takes place as a result of various issues such as deforestation, an increase in consumption by an increasingly larger population, uncontrolled land usage, etc. (Nadim et al., 2006). Landslides are primarily disasters that take place in mountainous and sloped areas around the world (Dikau et al., 1996). Soil drifts are caused by two main factors: human and environmental effects in general. Human factors can be controlled; however, it is very difficult to control factors originating from topography and soil structure (Turner et al., 2015). Thus, landslides cause disasters on a global scale each year. These disasters are increasing in number due to the incorrect usage of land. Landslides occur when gravitational and other types of shear stresses within a slope exceed the shear strength (resistance to shearing) of the materials that form the slope. The main reasons for the increase in landslide disasters are that vulnerable areas have become more susceptible to instability of the surface land because of extreme destruction of natural resources, deforestation, increased urbanization and uncontrolled land use. Triggering can occur faster because of short or long periods of heavy rain, earthquakes or subterranean activity (Lucier et al., 2014).

During landslide monitoring, a number of factors need to be continuously assessed: the extent of the landslide, detection of fissure structures, topography of the land and the rate of displacements that could be related to the fracture (Niethammer et al., 2010). Understanding the mechanism of landslides may be made easier by being able to measure the vertical and horizontal displacements. This is possible by forming a digital surface model (DSM) of the landslide area.

The calculation of displacements by differential Global Positioning System (DGPS), total station, airborne light detection and ranging (LIDAR) and terrestrial laser scanner (TLS) techniques have been used since the beginning of the 2000s (Nadim et al., 2006). Geodetic techniques, and especially GPS, are widely used with high precision for landslide monitoring (Brückl et al., 2006); however, geodetic techniques could be unsafe for the operator due to the risk of access to the landslide hazard area. In addition, local techniques may be time-consuming and costly for larger areas (Dewitte et al., 2008; Eker et al., 2018). These techniques use a large-scale point-based method of measurement, and point density often misses the desired frequency (Abellán et al., 2010). To remove these limitations, remote sensing techniques are used as alternatives for landslide monitoring (Eker et al. 2018). Additionally, remote sensing has been put into operation in combination with other techniques (Mantovani et al., 1996). There are several platforms that are used to monitor landslide occurrences via the method of remote sensing, where displacement data can be collected. These include remote sensing satellites, manned aerial vehicles, specially equipped land vehicles and, as a new method, unmanned aerial vehicles (UAV) (Rau et al., 2011). These UAVs, known as drones, are aerial vehicles that are able to fly without crew, either automatically or semi-automatically, based on aerodynamics principles. UAV systems have become popular in solving problems in various fields and applications (Saripalli et al., 2003; Tahar et al., 2011).

Nowadays, the use of UAVs is growing in engineering usage due to the characteristics of the vehicles; for example, low weight, small size, low cost and easy usage. UAVs can survey wide areas and reach dangerous areas; furthermore, several kinds of sensors can be embedded in them so as to convert UAVs into mobile measurement platforms (Daponte et al., 2017). In general, two types of mini-UAVs are currently available: multicopters and fixed-winged (Anders et al., 2013). According to

the sensor typology (digital camera, hyperspectral cameras, miniature radar, passive microwave radiometers and LIDAR sensors), they can be used for several application fields. In parallel with the developing technology, UAVs have been used in recent years in integration with the Global Positioning System (GPS), inertial measurement units (IMU) and high definition cameras; they have also been used in remote sensing (RS), digital mapping and photogrammetry in scientific studies. While satellites and manned aerial vehicles are able to gather location data in high resolutions of 20-50 cm/pixel, UAVs are able to obtain even higher resolutions of 1 cm/pixel, as they are able to fly at lower altitudes (Hunt et al., 2010). Indeed, UAV photogrammetry opens up various new applications in close-range photogrammetry in the geomatics field (Eisenbeiss, 2009). Monitoring landslides using UAV systems is an integrated process involving ground surveying methods and aerial mapping methods. All measurement devices that require details are integrated into UAVs, which fly at lower altitudes than satellites or planes. All positional data are collected safely from above, except for determining and measuring the control points (Nagai et al., 2008).

In this study, five flight missions carried out UAV-based monitoring of the Tokat industrial area landslide. High-resolution digital elevation models (DEMs), orthophotos and density point clouds were produced from UAV-based aerial photos. According to ground control points (GCPs), an average of  $\pm 3.5$  cm root mean square error (RMSE) was calculated for the models. A digital terrain model (DTM) and digital surface model (DSM) of the area was generated for each flight.

## 2. System Design

This study used the multicopter, which was produced by the department of Geomatics Engineering at Gaziosmanpaşa University (GOP) (Figure 1a and b). The designed multicopter consisted of a platform and camera systems.



Figure 1a. The UAV and environmental components



Figure 1b. The UAV in the air

### 2.1. UAV Platform

UAV platforms provide crucial alternative solutions for environmental research (Nex & Remondino, 2014). The UAV environmental components used in this study were integrated into the multicopter as seen in Figure 2. The platform had a blade-span of 0.80 m, height of 0.36 m, weight of 4.4 kg and operating weight of 5 kg. All sensors were placed on the carrying platform to achieve operating integrity. The carrying platform operated at the speed of 14 m/sec while shooting photos. The multicopter had a stabilized

camera gimbal to take nadir photos during the flight. The characteristics of the carrying platform are given in Table 1.



Figure 2. UAV environmental components

Table 1. Platform technical specifications

Specification	Technical Details
Weight	4.3 kg
Wing Span	74 cm
Payload	4 kg
Height	34 cm with GPS Antenna
Range	4 km
Endurance	30 min
Speed	14 m/sec
Maximum Speed	70 km - 30 mm /sec
Radio Control	433 MHz
Frame Transponder (FPV)	2.4 GHz
Telemetry Radio	868 MHz
GPS	5 Hz – 72 channels
Battery	6S li-po 25C 1600 Mah
Monitor	40 Channels 5.8 GHz DVR 7 inch LED system
Gimbal	Mapping Gimbal
Motors	35 x 15 Brushless Motor
Frame	22 mm 3K Carbon
ESC	60 Ampere 400 Hz
Prop	15 x 55 inch Carbon

Table 2. Camera specifications

Property	Technical Detail
Dimensions	4.72 x 2.63 x 1.78 in
Weight	10.05 oz. (Body Only) / 12.13 oz. (with battery and media)
Megapixels	12 MP
Sensor Type	APS-C
Sensor Size	APS-C type (23.5 x 15.6 mm)
Number of pixels (effective)	24.3 MP
Number of pixels (total)	Approx. 24.7 megapixels
ISO sensitivity (recommended exposure index)	ISO 100-25600
Clear image zoom	Approx. 2x
Digital zoom (still image)	L: Approx. 4x; M: Approx. 5.7x; S: Approx. 8x
LCD Size	3.0 in wide type TFT LCD
LCD Dots	921,600 dots
Viewfinder Type	0.39 in-type electronic viewfinder (color)
Shutter speed	Still images: 1/4000 to 30 sec, Bulb, Movies: 1/4000 to 1/4 (1/3 steps) up to 1/60 in AUTO mode (up to 1/30 in Auto slow shutter mode)
Flash sync. Speed	1/160 sec.

## 2.2. Camera System

In this study, a Sony ILCE-6000 E16 mm F2.8-16.0-6000x4000 (RGB) camera was used for collecting visible imagery. Table 2 shows the characteristics of the camera. The main controller of the UAV was programmed to shoot photos regularly, every two seconds. This way, the shutter of the camera was triggered at the desired frequency intervals.

The camera and the main flight controller card were connected using a special cable. Vibration isolation materials were used between the camera and the UAV to prevent the effects of flight vibrations on the camera. During the flight, all photos were taken in the RAW format and stored in the memory of the camera.

## 3. Study Area

This study was conducted in the landslide site at the organized industrial zone near a campus of Gaziosmanpaşa University. The area of the studied field was approximately 50 hectares. The coordinates of the landslide area used for the study are given as 40° 19' 20.8" N, 36° 30' 0.6" E. The study area is shown in Figure 3.

This study was carried out in order to monitor the landslides with UAV in Tokat Province. The study area was selected to track the landslides that began in the area where factories and industrial enterprises are located. There is a great landslide risk in this industrial area, it is a preexisting situation and if the motion continues or accelerates it could mean great danger for the nearby factories. For this reason, the movement needs to be monitored.

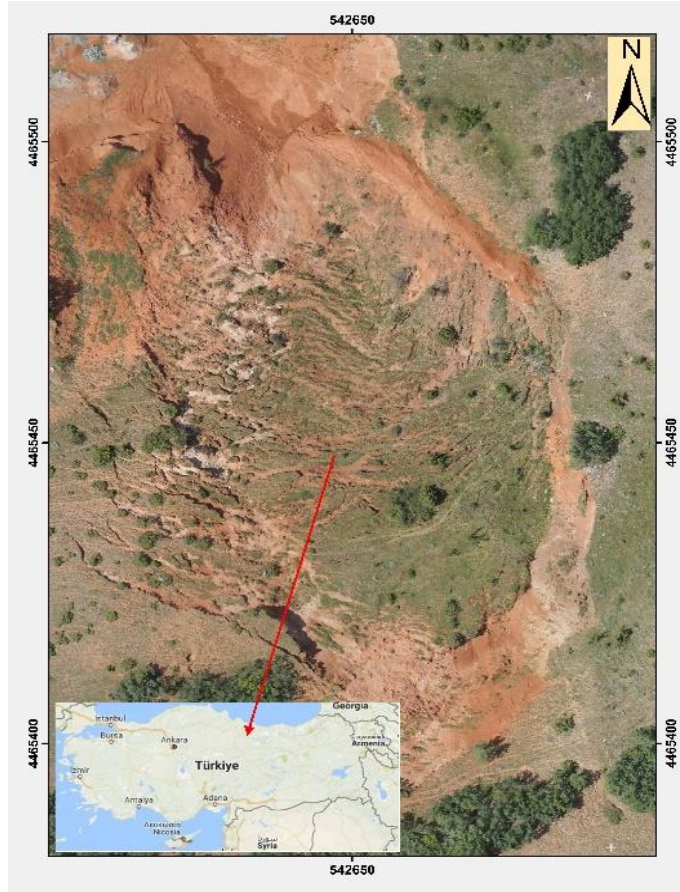


Figure 3. Location of the study area

### 3.1. Soil Properties of the Study Area

The oldest layer at the research area is Paleozoic aged metaophiolite (Metadunite, amphibolite/Metagabbro). The sedimentary layer, which is called eosin aged “Çekerek formation”, is over the metaophiolite layer. This formation consists of sandstone, pebble, silt and clay (Sumengen, 1998).

Soil samples were collected from three different locations at 0-0.2 and 0.2-0.4 m depths and analyzed for soil particle distribution using the Bouyoucos hydrometer method (Gee & Bauder, 1986). The fraction greater than 2 mm diameter was separated and reported as coarse material (Gee & Bauder, 1986). The dispersion ratio was calculated using Equation 1 (Middleton, 1930). The aggregate stability index was calculated by the wet sieving method (Yoder, 1936).

$$\text{Dispersion ratio} = \{D (\text{silt} + \text{clay}) / T (\text{silt} + \text{clay})\} \times 100 \quad (1)$$

Where D is dispersed silt + clay after 1 kg of oven-dried soil in a liter of distilled water was shaken 20 times; T is total silt + clay determined by the standard sedimentation method in a non-dispersed state. Some soil properties of the study area are presented in Table 3. The results of the mechanical analysis in most of the studied soils showed a high clay and silt and low sand content. The textural classes of the soil tests were determined as clay (C), clay loam (CL) and silt loam (SiL). The high clay and silt content of study area increased disaggregation by leading to imbalances in the moisture content of

different soil layers instead of aggregation. This effect may result in high runoff, soil loss and weathering processes. When the topsoil and subsoil layers were compared, the clay content of the topsoil layer decreased, the silt content was the same, and the sand content increased at study site one. At study site two, the higher clay and lower silt contents were detected more in the subsoil than in the topsoil. The same result was observed for study site three. Textural differences between the topsoil and subsoil created moisture differences in the soil layers, and this situation may result in large mass movements. In the study area, the coarse material varied between 4.2 and 31.0%, depending on the mass transportation.

Table 3. Soil properties and locations of the sample points

Study Site	Locations of Sample Points		Soil Depth (m)	Texture				Coarse Material %	Aggregate Stability %	Dispersion Ratio %
	Yi (m)	Xi (m)		Clay %	Sand %	Silt %	Class			
1	542643.22	4465499.28	0.0-0.2	40.0	28.7	31.3	CL	13.0	34.3	36.9
2	542651.962	4465489.02	0.2-0.4	37.5	31.2	31.3	CL	31.0	41.3	60.0
3	542640.56	4465571.35	0.0-0.2	50.0	11.2	38.8	C	4.2	13.9	57.8
4	542656.14	4465463.37	0.2-0.4	52.5	11.2	36.3	C	19.7	46.2	49.3
5	5426670.20	4465450.83	0.0-0.2	40.0	13.7	46.3	SiL	15.7	18.8	36.3
6	542661.27	4465428.60	0.2-0.4	42.5	13.7	43.8	SiL	6.6	13.1	47.9

To evaluate the forces of the soil resistance on the mass movement of the study area, aggregate stability and dispersion ratio indexes were used. The aggregate stability of the soil tests was under 46.2% and showed low aggregate stability with a high risk of soil movement. The dispersion ratio index indicated a sharp boundary between erodible and non-erodible soils, since a dispersion ratio greater than 10 indicated erodible soils and less than 10 indicated non-erodible soils. The dispersion values of the study area were greater than 10 with high erosion risk.

Table 4. Measurement periods and total rainfall amounts

Measurement Period	Date	Total Rainfall Amount (mm)
1	21 March 2016	21.9
2	11 April 2016	48.2
3	9 May 2016	63.0
4	1 June 2016	32.2
5	21 June 2016	

The study was carried out over five periods. The total precipitation was 21.9 mm between the first and second measurement periods, 48.2 mm between the second and third measurement periods, 63 mm between the third and fourth measurement periods, and

finally 32.2 mm between the fourth and fifth measurement periods. The most rainfall amount was observed between the third and fourth measurement periods, which are shown in Table 4.

### **3.2. 3D Ground Control Points**

A total of eight 3D GCPs were used in the study area. The GCPs were placed in a way so that they could be easily seen in photos taken from above, near the landslide site, but where future landslides would not affect them. All GCPs were placed as concrete blocks, which were topped with side wings with dimensions of 40 x 15 cm, so they could be easily detected in the computer environment. The geometrical distribution of the GCPs in the study area is given in Figure 4.

The 3D positional information of the GCPs was collected by the CORS-TR System (Mekik et al., 2011) using Topcon GR3 dual-frequency GNSS (Global Navigation Satellite System) receivers. Eight GCPs, which were well distributed over the data area, were set up in the landslide area (Figure 4). The positional information about the GCPs was collected using four dual-frequency geodesic GNSS receivers (Trimble, Topcon). Two hours of static GNSS measurements were analyzed in 3D using the Leica LGO V.8.3 software in connection with the TUSAGA-Active system. It was computed via static analysis at the datum of ITRF96 and epoch of 2005.00. With the dual-frequency receivers used, the horizontal sensitivity of the GCPs was found to be  $\pm 3\text{mm} + 0.5\text{ ppm}$ , while the vertical sensitivity was found to be  $\pm 5\text{ mm} + 0.5\text{ ppm}$ .

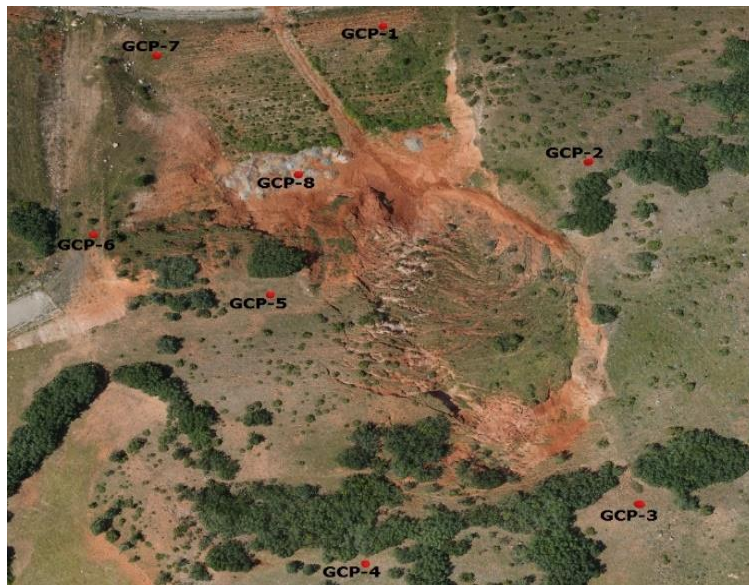


Figure 4. The geometric distribution of GCPs on the orthomosaic of study area

### **3.3. Flight Planning and Shooting of the Photos**

Flight plans were made following the GNSS measurements of the GCPs and obtaining their coordinates via analysis. The flights were carried out at five different periods following rainfall or snowfall (Table 4), where the landslide area was the most active. The flight dates and flight altitude information are given in Table 5. The flight plan for the study area was set within the Mission Planner software with vertical overlapping of 80%, horizontal overlapping of 65%, a flight altitude of 100 m and flying speed of 14 m/sec. A number of overlapping images were computed for each pixel of the

orthomosaics. The prepared flight plan was uploaded onto the UAV and the photos of the study area were obtained. The same input parameters were used in all periods for the flights and an average of 290 photos were taken. Meteorological factors were considered in shooting the aerial photos and the most suitable time periods were chosen for the flights.

Table 5. Dates of flights and flight altitude

Period	Flight Date	Flight Altitude (m)
1	February 17, 2016	100
2	March 22, 2016	100
3	April 9, 2016	100
4	June 10, 2016	100
5	July 21, 2016	100

### 3.4. Point Cloud, 3D Model and Orthomosaic Production

The photos obtained from each flight period were stored in a computer with an empty storage space of 100 GB and 8 GB of RAM. The photos were analyzed using the Pix4D software.

In the first stage, quality checks were performed for the images, dataset, camera optimization and GCPs; these were calculated and the software produced the quality check report for each of the time periods. The ground sampling distance (GSD) is the distance between two consecutive pixel centers measured on the ground. The bigger the value of the image GSD, the lower the spatial resolution of the image and the less visible details; GCPs were used to correct the geographical location of a project.

At least three GCPs are required to produce point cloud, orthomosaics and 3D models, which come from the desired datum from the photographs taken. Optimal accuracy is usually obtained with 5 - 10 GCPs. GCPs should also be well distributed over the data area. To orient and balance the point cloud and the 3D model, the Helmert transformation was applied. The transformation process was carried out with seven parameters, which were generated from a minimum of three GCPs and point cloud relations (Crosilla & Alberto, 2002; Niethammer et al., 2011; Watson, 2006).

In this study, the geographical location of the project was oriented and balanced through the use of eight GCPs. The RMS and GSD values of the GCPs are given in Table 6.

Table 6. GCPs' mean RMS errors

Periods	RMS (mm)	GSD (cm/in)
#1	±23	3.11 / 1.22
#2	±29	3.04 / 1.20
#3	±28	3.50 / 1.38
#4	±33	3.27 / 1.28
#5	±18	3.57 / 1.40

The second stage increased the density of 3D points of the 3D model, which were computed in the first stage. It represents the minimum number of valid re-projections of this 3D point to the images. Each 3D point must be projected correctly in at least two images. This option can be recommended for small projects, but it creates a point cloud with more noise. The minimum number of matches is three in Pix4D, as a default, but up to six can be chosen. This option reduces noise and improves the quality of the point cloud, but it can calculate fewer 3D points in the endpoint cloud.

In this project, the number of matches was taken as three. The second stage results are given in Table 7.

Table 7. Average density per m<sup>3</sup>

Periods	Average Density (per m <sup>3</sup> )	Grid DSM (cm)
#1	106.31	100
#2	104.15	100
#3	100.72	100
#4	128.15	100
#5	117.17	100

In the third stage, a DSM and an orthomosaic were formed for all periods. DSM formation was achieved by the triangulation method with 100 cm grid intervals. The aspect maps, showing the landslide motion direction for the first and last periods, were derived using the DSMs of periods 1 and 5. The differences between these maps can be seen, especially in the western and northern areas (Figure 5). This means that there was a movement between periods.

By using difference of DSM (DoD) between the first and the fifth flights' processed data, a DoD deformation map was generated. An elevation difference map was generated using the first and last flight and the map was compared with 73 sample points' elevation differences (Table 8). In addition, the first and last position differences of sample points were compared in the ArcGIS software with the difference map generated from the DoD. It can be seen in Figure 5 that the raised sample points (green) are in dark brown areas and the subsided sample points (red) are in yellow areas.

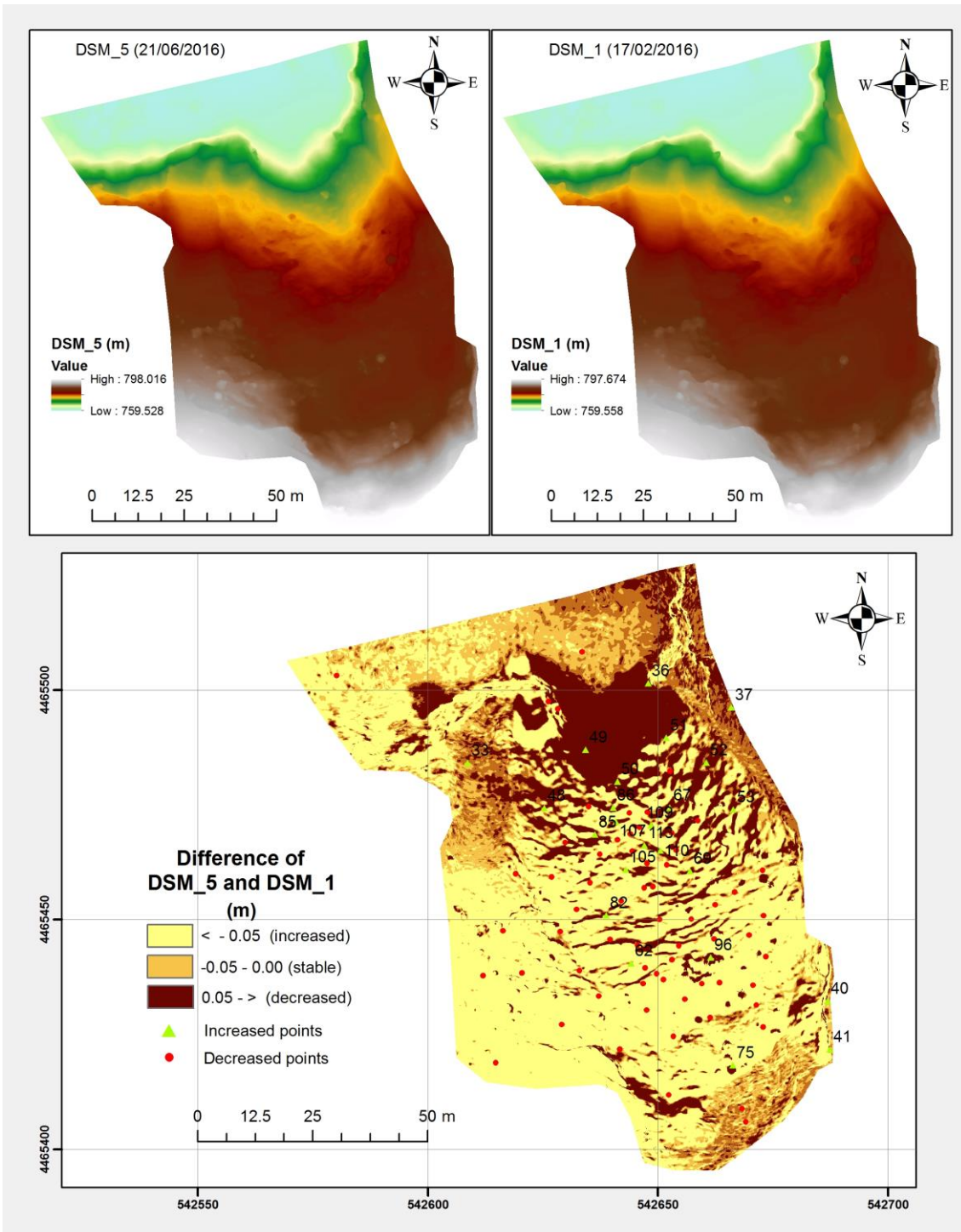


Figure 5. Difference of DSM (DoD) was generated between the first and the last flight data

### 3.5. Analysis of the Point Clouds, 3D Models and Orthomosaics

Seventy-three test points were determined in the study area in order to monitor the speed and direction of the landslide movement (Figure 6). These points, which represent the topography, were chosen from the clearly visible details in the model and the field.

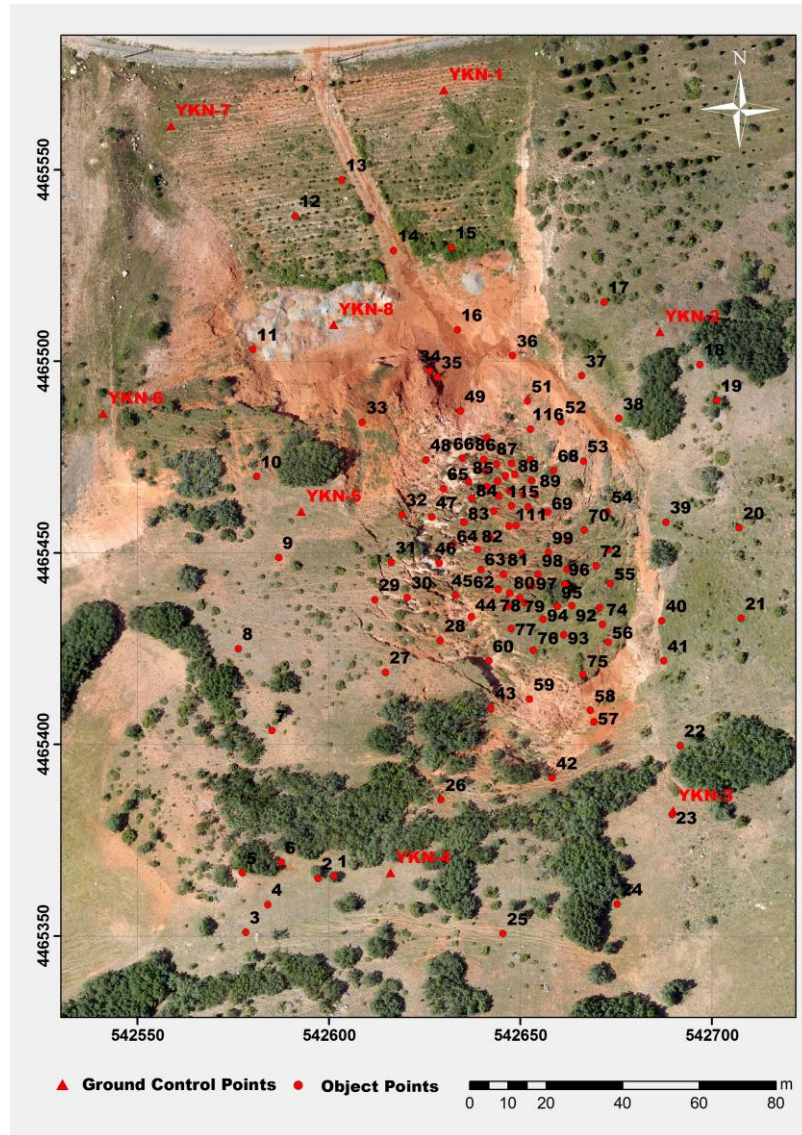


Figure 6. Ground control points (GCPs) and test points

The 3D position information, orthomosaics and DSMs of the test points were produced in each period. The 3D position data were compared consecutively. As a result of these comparisons, differential displacements were calculated between T2 and T1, T3 and T2, T4 and T3, T5 and T4, and are given in Figures 7, 8, 9 and 10. Additionally, Figure 11 provides a diagram showing the two-dimensional position shift ( $\Delta s$ ) and height ( $\Delta H$ ) changes between T5 and T1 (the last and the first periods).

According to these diagrams and Table 8:

- a) Points shown with a star (\*) are at the center of the area of motion and their positional displacement is higher than the median value ( $>21$  cm);
- b) Points shown without a star are outside the landslide area and their positional and height displacement values are lower than the median value ( $<21$  cm).

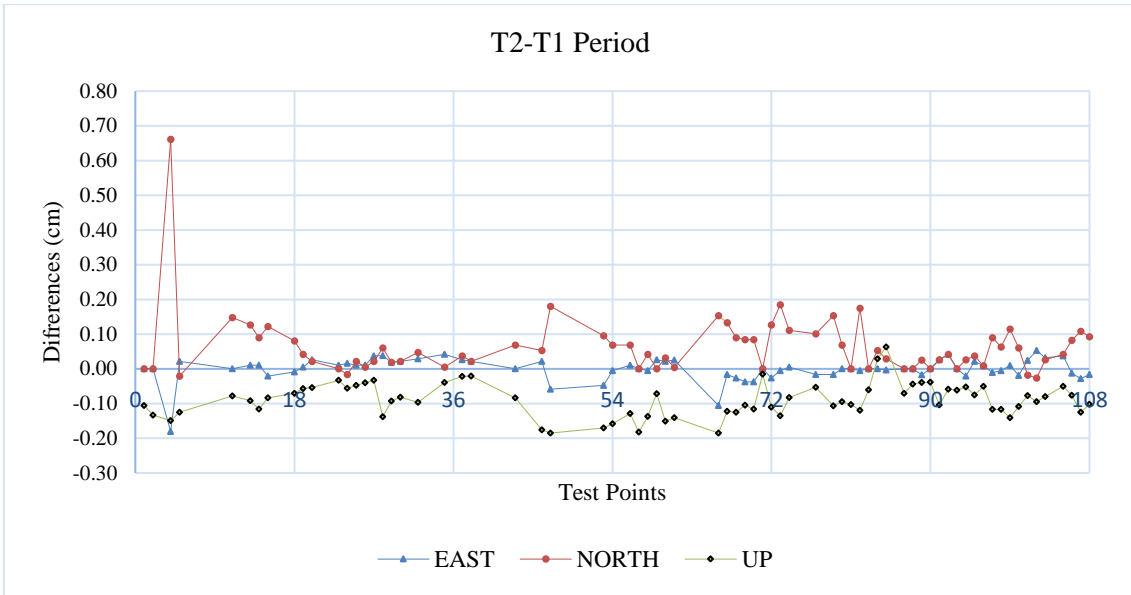


Figure 7. T2-T1 period differences

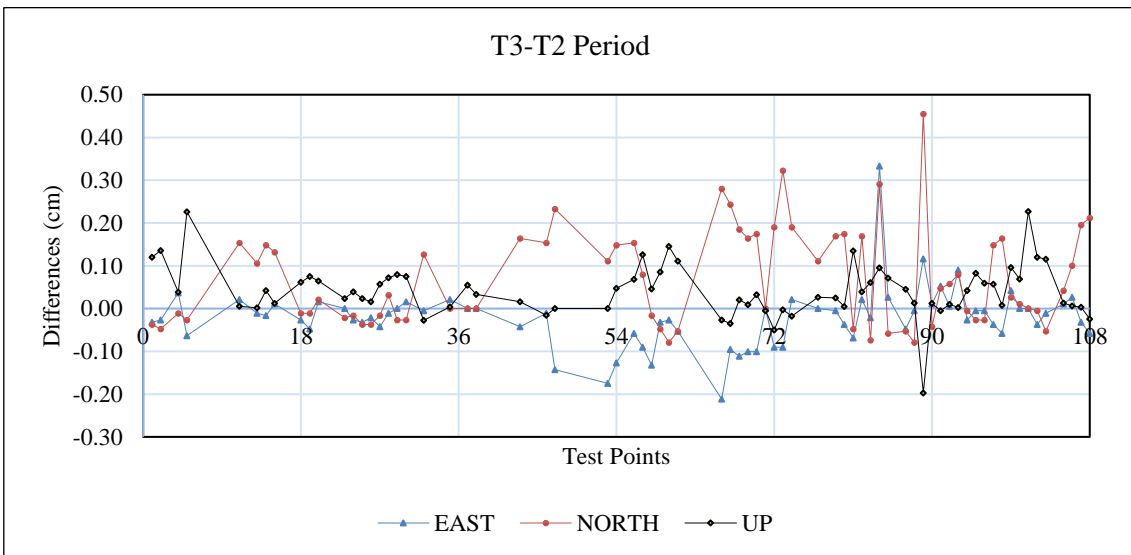


Figure 8. T3-T2 period differences

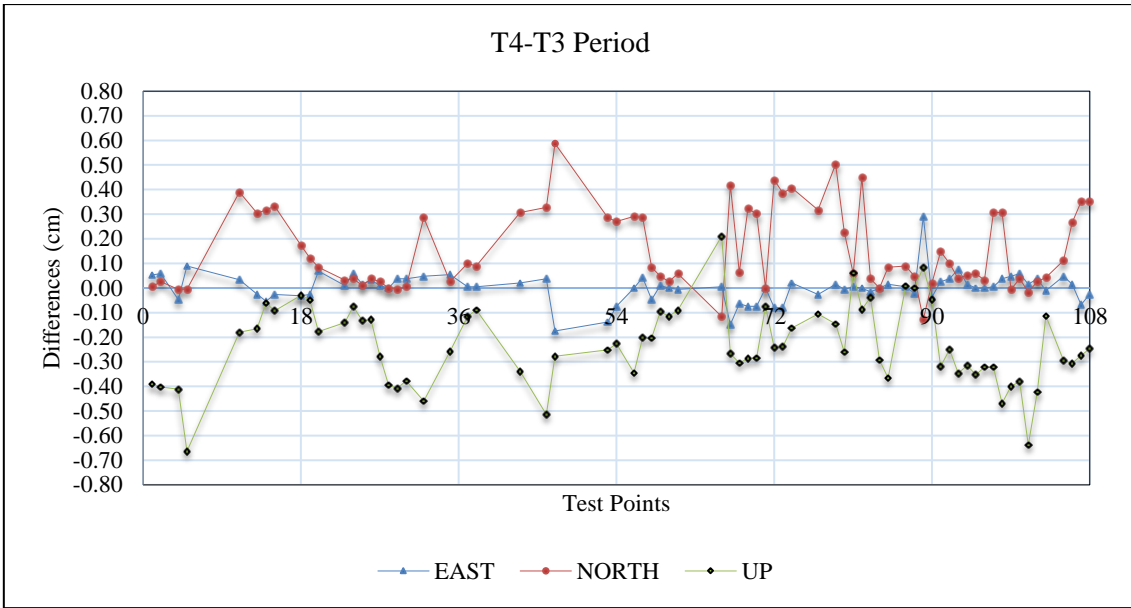


Figure 9. T4-T3 period differences

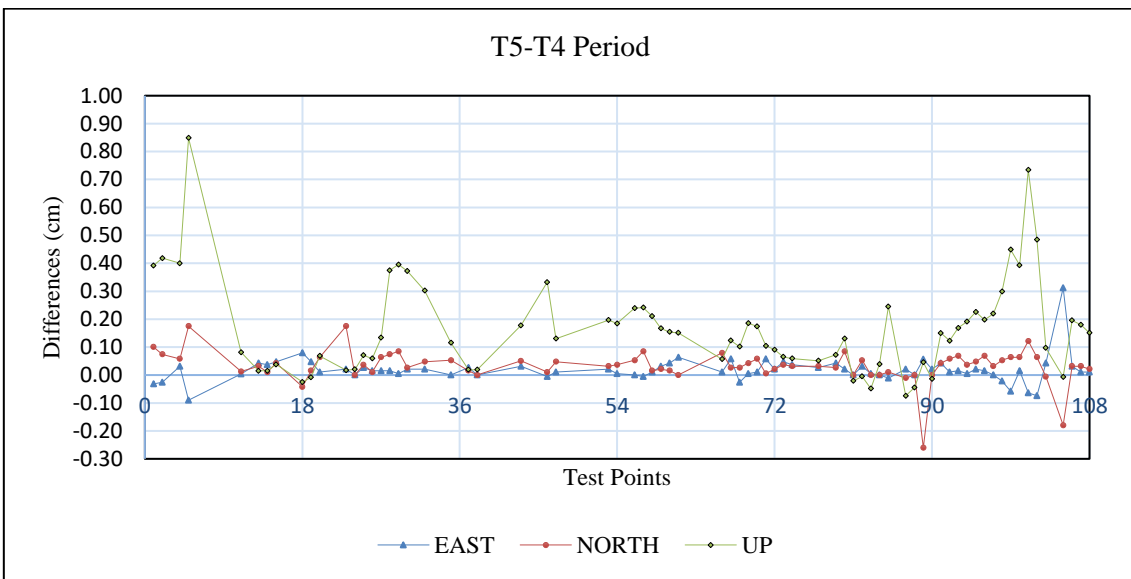


Figure 10. T5-T4 period differences

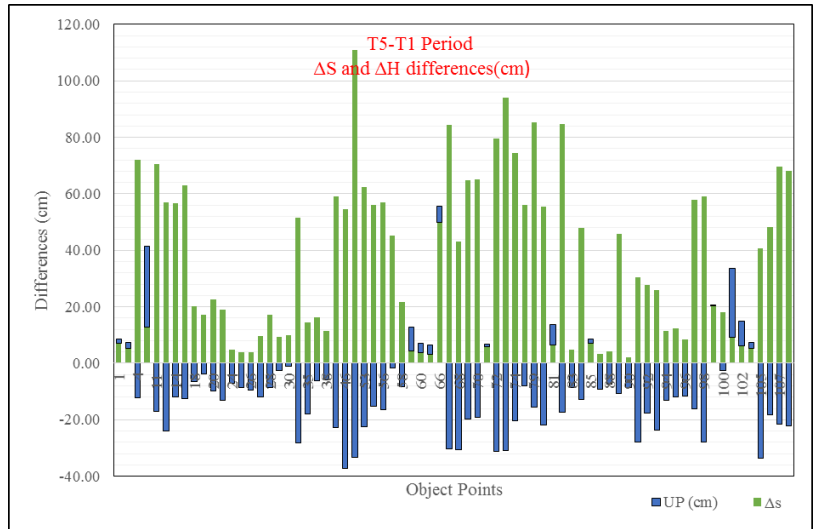


Figure 11. T5-T1 period ΔS and ΔH differences (cm)

The map in Figure 5 shows that the points with high positional displacement ( $\Delta S$ ) also have vertical displacement ( $\Delta H$ ) by 70%. The vertical and horizontal displacement correlation coefficient was calculated as  $\sigma=0.73$ . Thus, horizontal and vertical displacement of sample points is highly related to each other.

Not only the test points, but also the differences of the study area DSM's between the fifth and first flights were compared on the pixel unit. Results of the comparison are shown in Figure 5. Excavation and replacement of the earth material is shown in Table 8, and is also cross-checked with sample points. Material eroded areas (bigger than 5 cm) were colored with dark brown, stable areas were colored with light brown, and accumulated areas were colored with yellow.

Table 8. Vertical and horizontal displacements (cm) of sample points

Bigger than median movement value (>21 cm)			Smaller than median movement value (<21 cm)		
#Test Points	Displacement ΔH (cm)	Displacement Δs (cm)	# Test Points	Displacement ΔH (cm)	Displacement Δs (cm)
46*	-37.3	54.7	95	-12.0	12.2
105	-33.8	40.8	27	-12.0	9.7
47*	-33.2	111.0	14*	-11.9	56.7
72*	-31.2	79.7	96	-11.6	8.5
73*	-31.0	93.9	89	-10.6	45.7
68*	-30.7	43.0	20*	-9.7	22.6
67*	-30.2	84.5	26	-9.4	4.0
32	-28.2	51.6	87	-9.2	3.4
98*	-27.8	58.9	90	-8.7	2.2
91	-27.8	30.3	83	-8.7	4.9
13*	-24.0	56.9	28	-8.6	17.2
93*	-23.6	26.0	25	-8.6	3.8
43*	-22.9	59.1	58	-8.4	21.6
53*	-22.4	62.4	77	-8.0	8.0
108*	-22.1	68.2	88	-7.5	4.1
80*	-21.9	55.6	24	-7.2	4.8
107*	-21.7	69.7	18	-6.4	20.3
74*	-20.3	74.6	37	-6.3	16.4
69*	-19.6	64.8	38	-5.8	11.4
70*	-19.2	65.1	19	-3.8	17.1
106	-18.1	48.3	100	-2.5	18.0
35	-17.8	14.5	29	-2.5	9.5
92	-17.7	27.6	57	-1.7	45.3
82*	-17.4	84.8	30	-1.1	9.9
11*	-17.1	70.6	99	0.5	20.3
56*	-16.6	56.8	71	1.0	5.8
97	-16.1	57.8	85	1.5	7.2
79*	-15.5	85.3	1	1.6	6.9
54*	-15.3	56.1	103	1.8	5.4
23	-13.3	19.0	2	2.0	5.3
94	-13.2	11.4	61	3.1	3.2
84	-13.0	47.9	60	3.4	3.7
15*	-12.5	62.9	101	24.6	9.1
4*	-12.2	72.2	5	28.6	12.9

As a result of the positional movements obtained in the landslide area, point velocity vectors ( $V_x$ ,  $V_y$ ,  $V_z$ ) were calculated using Equation 2 below, and they are given in Table 9. It was found that the general characteristic surface movement of the landslide took place in the north-south direction (Figure 12).

$$V\{x, y, z\} = \frac{\Delta V\{x, y, z\}}{\Delta t} * 365 \quad (2)$$

Here:

$\Delta t$ : T5-T1 period time differences,

$\Delta V \{x, y, z\}$ : The difference between Cartesian coordinate components between the T5 and T1 periods.

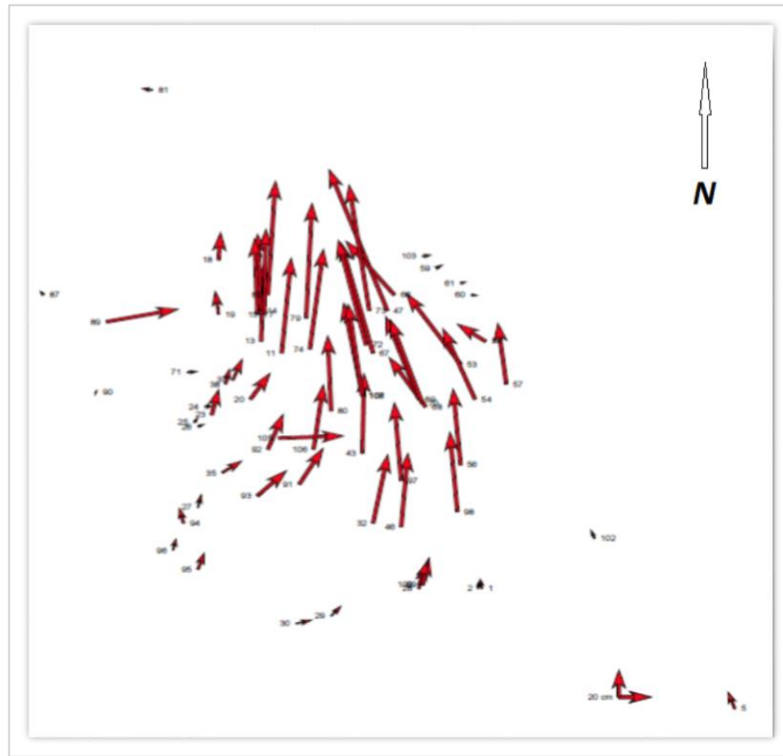


Figure 12. Characteristic surface movement of the landslide (m/year)

According to the velocity vectors, it may be seen that the landslide did not display a typical structure. The maximum movement was found to be  $v_x = -2.095$  m,  $v_z = -2.932$  m and  $v_y = 2.036$  m.

Table 9 and Figure 11 show that the test points numbered #47, 73, 79, 82, 67, 72, 74, 4, 11, 107, 108, 69 and 70 were at the center of the movement and had positional (2D) displacement ( $>50$  cm). The test points numbered #29, 101, 77, 96, 01, 85, 71, 81, 102, and 02 were outside the center of the movement and had positional (2D) displacement ( $<10$  cm).

Table 9. Test points annual velocity vectors

<i>#Test No</i>	<i>Vx (m/year)</i>	<i>Vy (m/year)</i>	<i>Vz (m/year)</i>	<i>#Test No</i>	<i>Vx (m/year)</i>	<i>Vy (m/year)</i>	<i>Vz (m/year)</i>
<i>1</i>	-0.068	-0.095	0.219	<i>68</i>	-0.851	-1.605	0.279
<i>2</i>	-0.064	-0.023	0.186	<i>69</i>	-1.111	-1.700	1.189
<i>4</i>	-1.214	-1.568	1.593	<i>70</i>	-1.122	-1.685	1.212
<i>5</i>	0.474	0.171	0.966	<i>71</i>	-0.108	0.172	0.036
<i>11</i>	-1.767	-1.035	1.480	<i>72</i>	-1.721	-2.010	1.362
<i>13</i>	-1.583	-1.084	0.968	<i>73</i>	-2.095	-2.077	1.772
<i>14</i>	-1.241	-0.996	1.233	<i>74</i>	-1.955	-1.063	1.505
<i>15</i>	-1.435	-1.001	1.387	<i>77</i>	-1.159	-0.913	1.306
<i>18</i>	-0.530	-0.333	0.392	<i>79</i>	-1.958	-1.268	1.908
<i>19</i>	-0.346	-0.343	0.364	<i>80</i>	-1.434	-1.139	0.981
<i>20</i>	-0.804	-0.064	0.285	<i>81</i>	0.265	-0.079	0.191
<i>23</i>	-0.707	-0.335	0.192	<i>82</i>	-2.009	-1.260	1.853
<i>24</i>	-0.261	0.013	-0.148	<i>83</i>	-0.052	-0.177	-0.293
<i>25</i>	-0.284	-0.118	-0.109	<i>84</i>	-1.588	0.275	0.615
<i>26</i>	-0.306	-0.066	-0.171	<i>85</i>	-0.147	0.016	0.206
<i>27</i>	-0.472	-0.255	-0.017	<i>87</i>	-0.200	-0.239	-0.136
<i>28</i>	-0.575	-0.234	0.246	<i>88</i>	-0.048	-0.151	-0.253
<i>29</i>	-0.311	0.037	0.133	<i>89</i>	-1.317	0.964	0.001
<i>30</i>	-0.268	0.214	0.043	<i>90</i>	-0.136	-0.124	-0.252
<i>32</i>	-1.716	-0.857	0.711	<i>91</i>	-1.379	-0.373	0.073
<i>35</i>	-0.776	-0.059	-0.181	<i>92</i>	-1.044	-0.355	0.289
<i>37</i>	-0.534	-0.140	0.263	<i>93</i>	-1.216	-0.108	-0.040
<i>38</i>	-0.380	-0.164	0.164	<i>94</i>	-0.429	-0.430	-0.002
<i>43</i>	-1.585	-1.112	1.050	<i>95</i>	-0.544	-0.240	0.037
<i>46</i>	-1.874	-1.190	0.605	<i>96</i>	-0.436	-0.238	-0.041
<i>47</i>	-1.863	-2.932	2.036	<i>97</i>	-1.307	-1.136	1.166
<i>53</i>	-0.734	-1.995	0.890	<i>98</i>	-1.564	-1.349	0.932
<i>54</i>	-0.865	-1.497	1.048	<i>99</i>	-0.437	-0.140	0.537
<i>56</i>	-1.285	-1.143	1.129	<i>100</i>	-0.479	-0.112	0.397
<i>57</i>	-0.747	-0.770	1.154	<i>101</i>	0.412	0.206	0.786
<i>58</i>	-0.051	-0.790	0.150	<i>102</i>	0.122	0.000	0.350
<i>59</i>	0.064	0.208	0.244	<i>103</i>	-0.089	0.163	0.069
<i>60</i>	0.007	0.165	0.063	<i>105</i>	-1.587	0.589	-0.723
<i>61</i>	-0.014	0.123	0.095	<i>106</i>	-1.385	-0.747	0.862
<i>66</i>	0.018	-1.281	1.183	<i>107</i>	-1.472	-1.579	1.336
<i>67</i>	-1.722	-2.124	1.498	<i>108</i>	-1.519	-1.493	1.297

## 4. Results

In the present study, five flight missions with a UAV were carried out over the landslide area. There was an interval of 155 days between the first and last UAV flights to take the images. A standard Sony ILCE-600 DSLR camera was used for this study. The horizontal and vertical sensitivity of the GCPs were found to be  $\pm 3 \text{ mm} + 5 \text{ ppm}$  and  $\pm 5 \text{ mm} + 5 \text{ ppm}$ , respectively. All flights were planned with 80% vertical and 65% horizontal overlooping and with 100 m flight altitude. An average of 190 images were taken for each flight to generate the models. Images had a GSD (cm/in) between 3.04/1.2-3.57/1.40 (Table 5). All orthophotos were generated using Pix4D, and all DEMs and orthophotos were produced at a resolution of 10 cm. The RMSE values for data from the first to last flights were 2.3, 2.9, 2.8, 3.3 and 1.8 cm, respectively (Table 6).

Each UAV flights lasted about 15 min and all image acquisition steps were completed in less than three hours. When compared to traditional field surveys, this duration was quite short. A high-density point cloud was generated for each mission with more than  $100 \text{ pts/m}^3$  (Table 7)

The UAV-based DSMs, orthophotos and point clouds were used for the monitoring of the landslide. Location information from 73 sample points was calculated by evaluating each post-flight photograph (Figure 9). The horizontal and vertical position differences of the sample points between consecutive flights were calculated and presented in Figure 10. Also, from the position differences obtained after the first and last flights, a positional difference graph was created for the sample points.

By using DoD between the first and the fifth flights' processed data, a DoD deformation map was generated. An elevation difference map was generated using the first and last flights, and the map was compared with 73 sample points' elevation differences (Table 8). In addition, the first and last position differences of sample points were compared in the ArcGIS software with the difference map generated from the DoD. It can be seen in Figure 5 that the raised sample points (green) are in dark brown areas and the subsided sample points (red) are in yellow areas.

Over the landslide area, a total of  $1330 \text{ m}^3$  of material was eroded, while  $480 \text{ m}^3$  of the material had accumulated. The map in Figure 5 shows that the points with high positional displacement ( $\Delta S$ ) also have vertical displacement ( $\Delta H$ ) by 70%. The vertical and horizontal displacement correlation coefficient was calculated as  $\sigma = 0.73$ . Thus, horizontal and vertical displacement of sample points is highly related to each other. According to the velocity vectors, it may be seen that the landslide did not display a typical structure. The maximum movement was found to be  $v_x = -2.095 \text{ m}$ ,  $v_z = -2.932 \text{ m}$  and  $v_y = 2.036 \text{ m}$ .

## 5. Conclusion

In this study, a case application of UAV-based photogrammetry was carried out for the landslide area. A standard digital camera was used to collect images for five UAV flights. The UAV-based DSMs, orthophotos and point clouds were used for the monitoring of the landslide. All orthophotos were generated using Pix4D. The UAV-DEM and orthophotos show great potential for analysis of landslide behavior. Landslides have a complex behavior with seasonal surface variations and episodic failures that are mostly triggered by intensive rainfall and increased pore-water pressures within the constituent geological materials. Each mission was completed by a 15-minute flight and process duration of approximately two hours for the landscape study. After processing, point cloud, DSM, DTM and orthophoto were prepared. This is a very short period of time when compared to conventional measurements. The same site can be measured with

conventional methods only within 3-4 hours and was only mappable in one day. In addition, it is always a great risk to make terrestrial measurements in landslide areas. Another disadvantage is that it is possible to make point-based measurements with conventional measurements.

In areas where landslides continue, some measurements may be needed to track the speed of motion. It is very dangerous and risky to make such measurements with traditional measurement methods. In these cases, movements should be monitored by remote measurement (remote sensing, photogrammetry and UAV) methods. Aerial photogrammetry and remote sensing techniques are not usually preferred because they are expensive. Measurements cannot be made at the desired time with these methods, and the sensitivity obtained with UAVs cannot be achieved.

One of the most important advantages of UAVs is that they can be utilized at almost any moment in time. This means that using UAVs is a flexible, fast and effective method for the acquisition of multitemporal data.

UAVs provide accuracy that with appropriate flight height and appropriate overlapping rates cannot be achieved with traditional observation methods; while all images have GSD values of approximately 1 cm, accuracy of 2-3 cm from DEMs, and orthophotocopies can be obtained.

The detail that should not be overlooked here is that it is a requirement that a sufficient number of GCP points must be measured with high accuracy.

## References

- Abellán, A., Calvet, J., Vilaplana, J. M., & Blanchard, J. (2010). Detection and spatial prediction of rockfalls by means of terrestrial laser scanner monitoring. *Geomorphology*, 119 (3–4), 162–171. <https://doi.org/10.1016/j.geomorph.2010.03.016>.
- Anders, N. S., Seijmonsbergen, A.C., & Bouten, W. (2013). Geomorphological change detection using object-based feature extraction from multi-temporal LIDAR data. *IEE Geoscience And Remote Sensing Letters*, 10, 1587-1591.
- Beguiria, S. (2006). Changes in land cover and shallow landslide activity: A case study in the Spanish Pyrenees. *Geomorphology*, 74, 196–206. doi: 10.1016/j.geomorph.2005.07.018.2006.
- Brückl, E., Brunner, F. K., & Kraus, K. (2006). Kinematics of a deep-seated landslide derived from photogrammetric, GPS and geophysical data. *Engineering Geology*, 88(3–4), 149–159. <https://doi.org/10.1016/j.enggeo.2006.09.004>.
- Calcaterra, D., Parise, M., Palma, B., & Pelella, L. (2000). The influence of meteoric events in triggering shallow landslides in pyroclastic deposits of Campania, Italy. In E. Bromhead, N. Dixon, M. L. Ibsen & A. A. Balkema (Eds.). *Proceedings of the 8th International Symposium on Landslides*, Cardiff, 1, 209–214.
- Calcaterra D, Parise M. (2005). Landslide types and their relationships with weathering in a Calabrian basin, southern Italy. *Bull Eng Geol Environ*, 64(2).193–207.
- Casagli, N., Dapporto, S., Ibsen, M. L., Tofani, V., & Vannocci, P. (2006). Analysis of the landslide triggering mechanism during the storm of 20th–21st November 2000, in Northern Tuscany. *Landslides* 3(1), 13–21. doi: 10.1007/s10346-005-0007-y.2006.
- Cevasco, A., Pepe, G., & Brandolini, P. (2014). The influences of geological and land use settings on shallow landslides triggered by an intense rainfall event in a coastal terraced environment. *Bulletin of Engineering Geology and the Environment*, 73(3), 859–875. doi: 10.1007/s10064-013-0544-x

- Cevasco, A., Brandolini, P., Scopesi, C., & Rellini, I. (2013). Relationships between geo-hydrological processes induced by heavy rainfall and land-use: The case of 25 October 2011 in the Vernazza catchment (Cinque Terre, NW Italy). *J Maps*, 9(2), 289–298. doi: 10.1080/17445647.2013.780188.2013.
- Crosta, G. B., & Frattini, P. (2003). Distributed modelling of shallow landslides triggered by intense rainfall. *Nat. Hazards Earth Syst. Sci.*, 3, 81–93.
- Crosilla, F., & Alberto, B. (2002). Use of generalised procrustes analysis for the photogrammetric block adjustment by independent models. *ISPRS Journal of Photogrammetry and Remote Sensing*, 56, 195–209.
- Daponte, P., De Vito, L., Mazzilli, G., Picariello F., & Rapuano, S. (2017). A height measurement uncertainty model for archaeological surveys by aerial photogrammetry. *Measurement*, 98, 192–198. <http://dx.doi.org/10.1016/j.measurement.2016.11.033>
- De Vita, P., Napolitano, E., Godt, J. W., & Baum, R. L. (2012). Deterministic estimation of hydrological thresholds for shallow landslide initiation and slope stability models: Case study from the Somma-Vesuvius area of southern Italy. *Landslides*, online first. doi: 10.1007/s10346-012-0348-2.2012.
- Dewitte, O., Jasselette, J. C., Cornet, Y., Van Den Eeckhaut, M., Collignon, A., Poesen, J., & Demoulin, A. (2008). Tracking landslide displacements by multi-temporal DTMs: A combined aerial stereophotogrammetric and LIDAR approach in western Belgium. *Engineering Geology*, 99(1-2), 11–22. <https://doi.org/10.1016/j.enggeo.2008.02.006>.
- Di Crescenzo, G., & Santo, A. (2005). Debris slides—rapid earth flows in the carbonate massifs of the Campania region (Southern Italy): Morphological and morphometric data for evaluating triggering susceptibility. *Geomorphology*, 66(1), 255–276. doi: 10.1016/j.geomorph.2004.09.015.
- Dikau, R., Brunsten, D., & Schrott, L. (1996). *Landslide recognition: Identification, movement and causes*. John Wiley and Sons.
- Eisenbeiss, H. (2009). *UAV photogrammetry*. (Unpublished doctoral dissertation). Institute of Geodesy and Photogrammetry, University of Technology, Zurich.
- Eker, R., Aydın, A., & Hübl, J., (2018) Unmanned aerial vehicle (UAV)-based monitoring of a landslide: Gallenzerkogel landslide (Ybbs-Lower Austria) case study. *Environ Monit Assess*, 190, 28 (pp:1914) <https://doi.org/10.1007/s10661-017-6402-8>
- Gee, G. W., & Bauder, J. W. (1986). *Particle size analysis. In methods of soil analysis*. Part 1 (2nd ed.). 383–411.
- Glade, T. (2003). Landslide occurrence as a response to land use change: a review of evidence from New Zealand. *Catena*, 51(3), 297–314.
- Guadagno, F. M., Martino, S., & Mugnozsa, G. (2003). Influence of man-made cuts on the stability of pyroclastic covers (Campania—southern Italy): A numerical modelling approach. *Environ Geol*, 43, 371–384.
- Guadagno, F. M., Forte, R., Revellino, P., Fiorillo, F., & Focareta, M. (2005). Geomorphology of the source areas of the flows involving the pyroclastic soils of Campania (southern Italy). *Geomorphology*, 66, 237–254.
- Guadagno, F. M., Forte, R., Revellino, P., Fiorillo, F., & Focareta, M. (2005). Some aspects of the initiation of debris avalanches in the Campania Region: the role of morphological slope discontinuities and the development of failure. *Geomorphology* 66, 237–254.
- Hunt, R., Hively, D., Fujikawa, S. J., Linden, D., Daughtry, C., & McCarty, G. (2010). Acquisition of NIR-green-blue digital photographs from unmanned aircraft for crop monitoring. *Remote Sensing*, 2, 290–305.

- Hungr, O., Leroueil, S., & Picarelli, L. (2014). The Varnes classification of landslide types, an update. *Landslides*, 11 (2), 167–194. DOI 10.1007/s10346-013-0436-y
- Lucier, A., Jong, S. M., & Turner, D. (2014). Mapping landslide displacements using structure from motion (SfM) and image correlation of multi-temporal UAV photography. *Progress in Physical Geography*, 38, 97-116.
- Iverson, M. R., & Major, J. J. (1986). Groundwater seepage vectors and the potential for hillslope failure and debris flow mobilization. *Water Resour Res*, 22, 1543–1548.
- Mantovani, F., Soeters, R., & Van Westen, C. J. (2016). Remote sensing techniques for land slide studies and hazard zonation in Europe. *Geomorphology*, 15(3-4), 213-225.
- Middleton, H.E. (1930). Properties of some soil which influence soil erosion. *USDA TECH. Bull*: 178.
- Moser, M., & Hohensinn, F. (1983). Geotechnical aspects of soil slips in alpine regions. *Eng Geol*, 19,185–211.
- Moser, M. (2002). Geotechnical aspects of landslides in the Alps. In J. Rybar, J. Stemberk & P. Wagner (Eds.). *Landslides. Proceedings of the 1st European conference on landslides* (pp. 23–43). Lisse, Netherlands: Swets & Zeitlinger.
- Mekik, C., Yildirim, O., & Bakici, S. (2011). The Turkish real time kinematic GPS network (TUSAGA-Aktif) infrastructure. *Scientific Research and Essays*, 6(19), 3986-3999.
- Montgomery, D. R., & Dietrich, W. E. (1994). A physically based model for the topographic control on shallow landsliding. *Water Resour Res*, 30, 1153–1171.
- Nadim, F., Kjekstad, O., Peduzzi, P., et al. (2006). Global landslide and avalanche hotspots. *Landslides*, 3, 159-173.
- Niethammer, U., Rothmund, S., James, M. R., Travelletti, J., & Joswig, M. (2010). *UAV based remote sensing of landslides*". In proceedings of the *International Archives of Photogrammetry, Remote Sensing and Spatial Information Sciences, Commission V Symposium*, June 21-24, Newcastle Upon Tyne.
- Nex, F., & Remondino, F. (2014). UAV for 3D mapping applications: A review. *Appl. Geomatics.*, 6, 1-15. DOI:10.1007/s12518-013-0120-x.
- Niethammer, U., Rothmund, S., Schwaderer, U., Zeman, J., & Joswig, M. (2011). Opensource image processing tools for low cost UAV based landslide investigations. In Proceedings of the *International Archives of Photogrammetry, Remote Sensing and Spatial Information Sciences*, ISPRS, September 14-16, Zurich.
- Nagai, M., Chen, T., Ahmed, A., & Shibasaki, R. (2008). UAV borne mapping by multi sensor integration. *The International Archives of the Photogrammetry, Remote Sensing and Spatial Information Sciences*, 37, Part B1, 2008 July 3-11, Beijing.
- Rau, J. Y., Jhan, J. P., Lo, C. F., & Lin, Y. S. (2011). Landslide mapping using imagery acquired by a fixed –wing UAV. Proceedings of ISPRS Workshop, *International Archives of Photogrammetry Remote Sensing and Spatial Information Sciences*, 38(1)/C22, September 14-16, Zurich.
- Saripalli, S., Montgomery, J. F., Sukhatme, G. S. (2003). Visually guided landing of an unmanned aerial vehicle. *IEEE Transaction on Robotics and Automation*, 19, 371-380.
- Sumengen, M. (1998). *Turkish 1/100000 scaled geological map reports*. Ankara, Turkey: General Directorate of Mineral Research Ankara. [In Turkish].
- Tahar, K., Ahmad, A., Akib, W. A. & Udin, W. S. (2011). Unmanned aerial vehicle technology for large scale mapping. ISG & ISPRS Conference, May 10-11, Munich.
- Turner, D., Lucieer, A., & DeJong, S. M. (2015). *Time series analysis of landslide dynamics using an unmanned aerial vehicle (UAV)*. *Remote Sensing*, 7, 1736-1757.
- Yoder, R. E. (1936). A direct method of aggregate analysis of soils and a study of the physical nature of erosion losses. *J. Am. Soc. Agric.*, 28, 337–351.

Watson, G. A. (2006). Computing helmert transformations. *Journal of Computational and Applied Mathematics*, 197(2), 387-394.